



# Rapid recycling of subducted sedimentary carbon revealed by Afghanistan carbonatite volcano

Forrest Horton  

**The fate of carbon subducted to mantle depths remains uncertain, yet strongly influences the distribution of terrestrial carbon on geologic timescales. Carbon fluxes into subduction zones are exceptionally high where downgoing plates contain thick sedimentary fans. This study uses volcano geochemistry to assess sedimentary carbon recycling in the high-flux Makran subduction zone, where the Arabian plate subducts northward beneath Eurasia. On the basis of strontium isotope geochemistry and  $^{40}\text{Ar}$ – $^{39}\text{Ar}$  geochronology, I show that a portion of the submarine Indus Fan entered the Makran Trench, melted and ascended as magmas that erupted in southern Afghanistan. The resulting volcano, composed primarily of carbonate minerals, formed at approximately 3.8 million years ago. The  $^{87}\text{Sr}/^{86}\text{Sr}$  ratios of the lavas indicate that their magmatic precursors were derived from marine sediments deposited at  $28.9 \pm 1.4$  Ma. This implies that sedimentary carbon was subducted to and returned from mantle depths in less than 27 million years, indicating that magmas can efficiently recycle sedimentary carbon from subducting slabs to the overlying plate.**

The efficiency of carbon recycling in subduction zones has profound implications for Earth's climate<sup>1</sup>. Some fraction of the carbon entering subduction zones is released from subducted slabs via mechanical removal, metamorphic decarbonation and melting. The remainder recycles to lithospheric reservoirs in buoyant diapirs<sup>2</sup> and melts<sup>3,4</sup> or enters the convecting mantle<sup>5</sup>. Subducted carbon that does not return to near-surface reservoirs may remain isolated from the biosphere for billions of years<sup>6,7</sup>. Globally, the carbon flux into subduction zones appears to exceed the combined outputs from arc volcanoes and diffuse venting<sup>6,8</sup>. This may be indirect evidence that deep Earth reservoirs serve as carbon sinks on geologic timescales. Yet, the fate of deeply subducted carbon remains an enigmatic aspect of the global carbon cycle.

The Makran subduction zone, with the highest carbon flux per unit length along the trench of any modern subduction zone<sup>9</sup>, is uniquely well suited for investigating carbon recycling in a high-flux setting. The Makran continental margin is dominantly accretionary<sup>10</sup> and includes a Neogene–Quaternary volcanic arc that consists of three volcanic centres in Iran and Pakistan<sup>11</sup>. Here, I present evidence that a carbonatite volcano in southern Afghanistan is a hitherto unrecognized eastern limb of the Makran volcanic arc. This volcano is proof that carbonatitic melts, theoretically generated in subduction zones at postarc depths (>140 km)<sup>6,12</sup> but seldom attributed to volcanic arc processes<sup>13</sup>, can be voluminous enough to efficiently recycle subducted sedimentary carbon to the lithosphere. Isotope geochemistry and geochronology constrain the timing of sedimentary deposition and eruption, respectively, and imply that subducted carbon can return to shallow reservoirs on much shorter timescales than previously thought<sup>14–16</sup>.

## The Makran subduction zone and volcanic arc

As the Eurasian and Arabian plates converge, Arabian oceanic crust enters the Makran subduction zone at a rate of approximately 30 mm per yr (ref. <sup>17</sup>). The Arabian plate carries Indus Fan sediments—the thickest sequence of sediments (5–7.5 km) entering any subduction zone—into the Makran Trench, causing an unusually shallow grade of subduction and an exceptionally large

accretionary prism<sup>18</sup>. The crustal wedge extends ~300 km north from the trench, increasing in age from unconsolidated Quaternary period sediments through imbricated Miocene epoch ophiolites and metasediments<sup>10</sup>.

As previously defined, the Makran volcanic arc consists of three Neogene–Quaternary volcanic centres—Bazman, Taftan and Koh-i-Sultan—along an east-northeast linear trend oblique to the trench (Fig. 1)<sup>11</sup>. Lavas erupted at these locations have basaltic to rhyolitic compositions and fall along calc-alkaline differentiation trends<sup>19</sup>. Subduction-zone geometry varies from east to west: subduction in the east is shallower near the coast<sup>20</sup> and steeper at greater depths<sup>21</sup> compared with subduction in the west. This asymmetry might be due to oceanic lithosphere subduction in the east and continental lithosphere underthrusting in the west<sup>22</sup>.

The Khanneshin carbonatites (Extended Data Fig. 1) erupted through Neogene sedimentary rocks (Extended Data Fig. 2) of the Sistan Basin, southern Afghanistan, along intersecting regional faults<sup>23</sup>. The core of the 4-km-wide main vent consists of calcite-rich medium- to coarse-grained carbonatite (sövite) ringed by agglomeritic ankerite–barite carbonatite (Extended Data Figs. 3–5)<sup>24</sup>. Both units contain abundant mica-rich xenoliths of metasomatized wall rock (fenite) and are crosscut by fine-grained carbonatite (alvikite) dikes. A volcano-sedimentary apron extends radially 3–5 km from the main vent and is intruded by many late-stage dikes and volcanic plugs, the youngest of which are phonolitic. Aeromagnetic surveys suggest that as many as eight other minor alkaline igneous centres with unknown ages and compositions may be buried beneath Holocene epoch sands<sup>23</sup>. Unlike most volcano-forming carbonatites<sup>25</sup>, however, the Khanneshin volcano does not appear to be accessory to silicic volcanism.

## Chronologic and geochemical constraints

Some geochemical data exist for the Khanneshin carbonatites<sup>23,26,27</sup>. This study adds two critical results:  $^{40}\text{Ar}$ – $^{39}\text{Ar}$  geochronology that establishes the timing of Khanneshin volcanism, and strontium isotopic constraints for Khanneshin rocks (see Supplementary Information for sample descriptions).

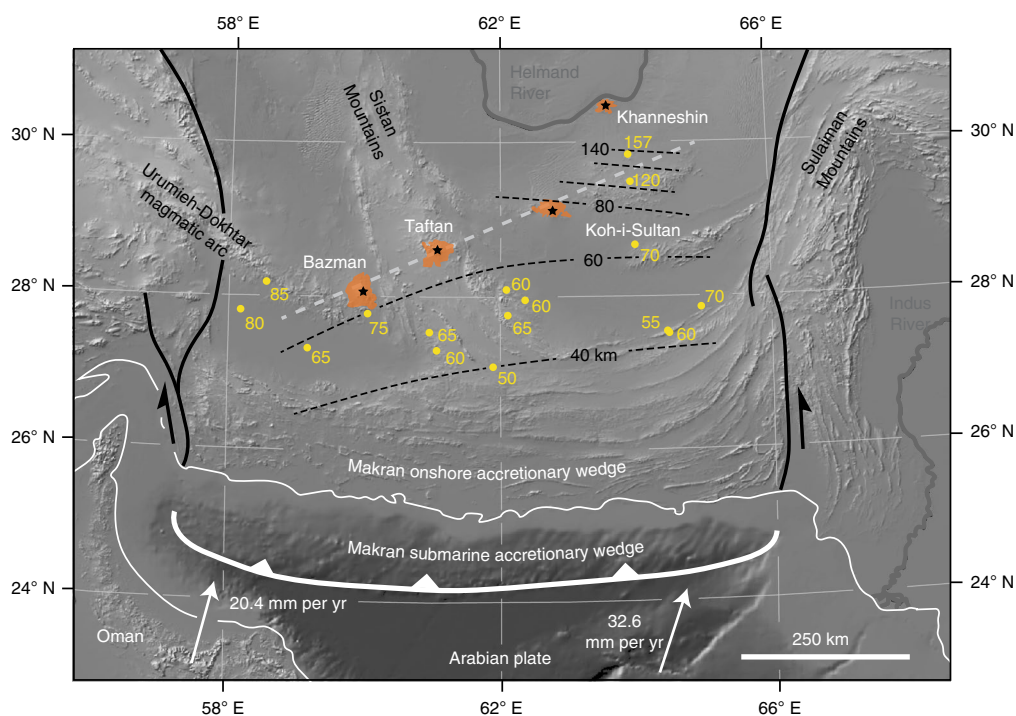


**Fig. 1 | Map of the Makran subduction zone and volcanic arc.** Earthquake focal mechanisms<sup>17</sup> (yellow symbols with approximate depths in kilometres) in the subducting crust indicate that the slab passes beneath the three western volcanic centres<sup>11</sup> (orange). The approximate slab-top depth is contoured by black dashed lines based on earthquake focal mechanism depths. The Khanneshin volcano is slightly north of the linear trend (light grey dashed line) defined by the calc-alkaline volcanic arc centres.

**<sup>40</sup>Ar–<sup>39</sup>Ar geochronology.** Sövite sample RT-10K-09, which was inferred to be the least geochemically evolved because it has light carbon, oxygen and thallium isotopic compositions<sup>27</sup>, was selected to represent the main stage of eruption. Unlike other mica-bearing Khanneshin samples, the coarse-grained phlogopite in RT-10K-09 is not associated with fenite xenoliths. Step heating experiments on three phlogopite aliquots yielded <sup>40</sup>Ar–<sup>39</sup>Ar plateau ages of 3.54, 3.74 and 3.83 Ma that consisted of 63, 45 and 35% of the total <sup>39</sup>Ar released, respectively (Extended Data Fig. 6). The analytical uncertainty for each date is 0.02–0.04 Ma and the full external uncertainty for each analysis is 0.20 Ma. All three <sup>40</sup>Ar–<sup>39</sup>Ar ages agree within uncertainty and could represent a single argon closure age between 3.74 and 3.63 Ma. Alternatively, the oldest date (3.83 Ma) may represent the eruption age of the sövite if the younger dates record partial resetting caused by subsequent eruptive episodes that reheated the sample and caused argon loss.

**Strontium isotopes.** Twenty Khanneshin carbonatites have relatively homogeneous <sup>87</sup>Sr/<sup>86</sup>Sr ratios (Extended Data Table 1), ranging from  $0.707919 \pm 7$  (RT-11K-06) to  $0.708061 \pm 8$  (KHAN-3) and with a mean of  $0.708004 \pm 36$  (1 s.d.,  $n = 20$  rocks). This is comparable to previous results for Khanneshin rocks<sup>26</sup> and confirms that there is little strontium isotopic variability across the central vent of the volcano. The brecciated sandstone (represented by sample FH-10K-10), through which the carbonatitic lavas erupted, has a <sup>87</sup>Sr/<sup>86</sup>Sr ratio indistinguishable from the carbonatites; this value probably represents the isotopic composition of calcite veins (Extended Data Fig. 2) rather than the sedimentary protolith (see Supplementary Information).

### Evidence for rapid carbon recycling

Three lines of evidence indicate that the Khanneshin magmas were products of active subduction. First, the Khanneshin volcano is spatially and temporally associated with the Makran volcanic arc.

Earthquake focal mechanisms within the subducting slab (Fig. 1) extend to 157 km depth<sup>17</sup> and the deepest earthquake occurred less than 70 km to the south-southeast of the Khanneshin volcano<sup>28</sup>. This suggests that the slab passes beneath the volcano ~700 km north of the trench at a depth of ~180 km. The age of the Khanneshin volcano is bracketed by silicic volcanism at the Bazman (4.6 to <0.6 Ma), Taftan (6.95 to <0.71 Ma) and Koh-i-Sultan (<2.5 Ma) volcanoes<sup>29</sup>, which are indisputably part of the Makran volcanic arc. Furthermore, the Khanneshin volcano is only slightly north of the linear trend defined by the other volcanoes (Fig. 1). These observations suggest that the Khanneshin volcano is the easternmost manifestation of the Makran volcanic arc.

Second, sediments on the downgoing slab beneath the Khanneshin volcano could be fertile sources of carbonatitic melt. In the Makran subduction zone, the slab–mantle interface may not heat to 450 °C until reaching a depth of 75 km (ref. <sup>30</sup>). Heating may accelerate as the slab passes through the lithosphere–asthenosphere boundary, located ~150 km beneath the Khanneshin volcano<sup>31</sup>. When heated above ~700 °C, sediment layers thicker than 1 km are prone to forming buoyant diapirs<sup>2</sup>, which undergo partial melting and efficient decarbonation as they ascend into the mantle wedge<sup>32</sup>. Sediments can also be convectively transferred from the slab into the mantle wedge<sup>3</sup>. During burial, subducted Indus Fan material (calcareous ooze and clay-rich terrigenous turbidites<sup>33</sup>) would have consolidated and metamorphosed into carbonated pelites. At 950–1,050 °C and 3–5 GPa (refs. <sup>3,34</sup>), these lithologies can produce carbonated alkali-rich melt. Such conditions are plausible near the top of the subducting slab and in the mantle wedge. Carbon- and alkali-rich melt released from metasediments may separate into immiscible carbonatitic and silicate magmas during ascent. The buried igneous centres near the Khanneshin volcano<sup>23</sup> could represent conjugate silicate magmas. Thus, there are viable mechanisms by which carbonatitic melt might be generated beneath the Khanneshin volcano. Exceptionally high rates of carbonatitic melt

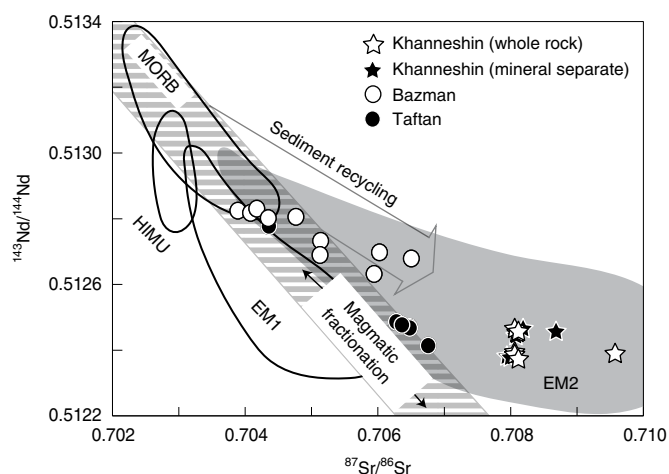


**Fig. 2** |  $^{143}\text{Nd}/^{144}\text{Nd}$  and  $^{87}\text{Sr}/^{86}\text{Sr}$  ratio systematics of the Makran arc.

The neodymium and strontium isotope compositions of Makran volcanic arc samples testify to sediment recycling. Khanneshin lavas fall along the same Enriched Mantle 2 trend as Bazman and Taftan samples<sup>11,29</sup>; this trend cannot be explained by magmatic fractionation of Rb/Sr and Sm/Nd from mid-ocean-ridge basalt values (hatched area) and indicates sediment recycling<sup>35</sup>. The Khanneshin data are from ref. <sup>26</sup> and mantle geochemical fields are from ref. <sup>36</sup>. EM1, Enriched Mantle 1; EM2, Enriched Mantle 2; HIMU, high  $\mu$  (where  $\mu = ^{238}\text{U}/^{204}\text{Pb}$ ); MORB, mid-ocean-ridge basalt.

generation in the Makran subduction zone could be facilitated by (1) an abnormally high sediment flux, (2) the abundant carbonate in the sediments (they can contain >50%  $\text{CaCO}_3$  (ref. <sup>33</sup>)) and (3) efficient carbon subduction past typical forearc depths<sup>9</sup>.

Third, the Khanneshin lavas contain geochemical evidence of crustal recycling. Their trace element patterns are consistent with the immiscible separation of carbonatitic magma from silicate magma derived from the melting of Indus Fan material (see Extended Data Table 2, Supplementary Information and Extended Data Fig. 7). Isotopically, Khanneshin, Bazman and Taftan volcanic rocks fall along a common  $^{143}\text{Nd}/^{144}\text{Nd}$  and  $^{87}\text{Sr}/^{86}\text{Sr}$  ratio trend (Fig. 2) that diverges from trends attributable to the magmatic fractionation of rubidium/strontium and samarium/neodymium. Such strontium–neodymium decoupling has long been viewed as evidence of sedimentary recycling<sup>35</sup>. The Makran arc values (including the Khanneshin lavas) fall within the Enriched Mantle 2 array, which is likewise attributed to a recycled sediment component<sup>36</sup>. Thallium isotope compositions of Khanneshin lavas also attest to ocean-crust recycling, despite being strongly influenced by wall rock interactions<sup>27</sup>. Interestingly, the  $^{206}\text{Pb}/^{204}\text{Pb}$ ,  $^{207}\text{Pb}/^{204}\text{Pb}$  and  $^{208}\text{Pb}/^{204}\text{Pb}$  ratios (18.9, 15.6 and 40.0, respectively) of Khanneshin carbonatites<sup>26</sup> are very similar to average Indus River potassium feldspars<sup>37</sup>; Khanneshin lavas may have inherited this signature from continental detritus transported by the Indus River.

Elsewhere, carbonatites may contain ancient recycled material from lithospheric reservoirs reactivated by backarc extension, mantle wedge flow or ascending magmas. That is not a likely source of the recycled sedimentary component in the Khanneshin lavas. The Afghan block, through which Khanneshin magmas erupted, formed by the accretion of one or more Gondwana microcontinents to Asia by the Early Cretaceous<sup>38</sup>. Southern Afghanistan, as part of the vast Alpine–Himalayan orogen, should have young lithospheric mantle (probably less than 50 Ma (ref. <sup>39</sup>)) and is far from cratons that could serve as long-lived geochemical reservoirs. Thus, and for the reasons outlined above, that is (1) spatiotemporal associations with arc volcanism and the Makran slab, (2) viable mechanisms for voluminous carbonatitic melt production and (3) geochemical

evidence for recycled sedimentary material, Khanneshin carbonatites can be viewed as products of Makran subduction.

Sediments in the Makran subduction zone are the most likely source of Khanneshin magmas. Because Khanneshin lavas have very high strontium concentrations (multiple wt% in most cases), substantial strontium isotopic contamination during magma ascent seems unlikely, even if Palaeozoic era or older rocks exist beneath the volcano. As noted above, the mantle lithosphere beneath the volcano is young, so remobilization of strontium implanted in the subcontinental lithosphere before the initiation of the Makran subduction zone also seems unlikely. Instead, the  $^{87}\text{Sr}/^{86}\text{Sr}$  measured in Khanneshin rocks probably reflects the isotopic composition of subducted Indus Fan material. The Indus River initiated during the Eocene epoch shortly after the India–Asia collision began. Much of the resulting submarine fan formed during the Palaeogene period<sup>40</sup>. If the Khanneshin lavas inherited the  $^{87}\text{Sr}/^{86}\text{Sr}$  compositions of their sedimentary precursors, the monotonic increase in marine sedimentary carbonate  $^{87}\text{Sr}/^{86}\text{Sr}$  since 40 Ma can be used as a chronometer (Fig. 3). Average marine carbonates<sup>41</sup> have  $^{87}\text{Sr}/^{86}\text{Sr}$  compositions overlapping with mean Khanneshin carbonatites ( $0.708004 \pm 36$ ) only once since 200 Ma. The  $^{87}\text{Sr}/^{86}\text{Sr}$  range in Khanneshin lavas suggests that their source rocks had a mean deposition age of  $28.9 \pm 1.4$  Ma, which coincides with early Indus Fan growth. Assuming that the  $^{40}\text{Ar}$ – $^{39}\text{Ar}$  plateau ages (3.83–3.54 Ma) record the main stage of volcanism, 24–27 Myr passed between deposition and eruption. The current length of the slab from the trench to beneath the volcano is ~700 km. However, the trench has migrated 140 km southwards since the mid-Miocene<sup>42</sup>, so the slab segment currently beneath the volcano travelled only ~560 km since entering the trench. At the current rate of 32.6 mm per yr (ref. <sup>17</sup>), subduction to

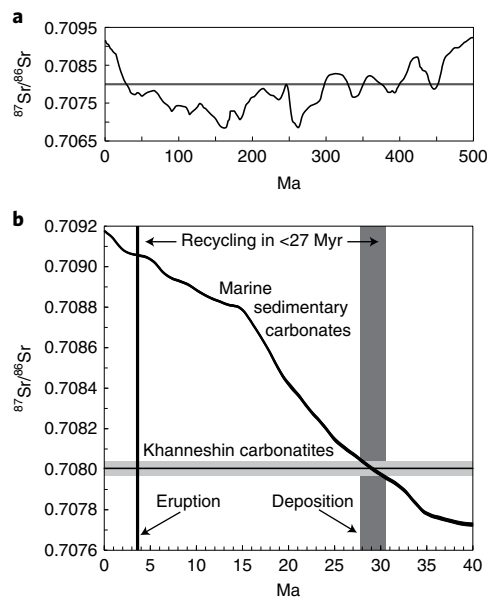


**Fig. 3** | Strontium isotopic evidence of rapid sediment recycling. **a**, The  $^{87}\text{Sr}/^{86}\text{Sr}$  of Khanneshin carbonatites versus average marine sedimentary carbonates<sup>41</sup>. The horizontal black line and the bounding light grey area represent the mean ( $n = 20$  rocks) and  $\pm 1$  s.d., respectively, for the Khanneshin carbonatites. Since 500 Ma, average marine sedimentary carbonate compositions have equalled that measured in the Khanneshin carbonatites nine times, but only once since 200 Ma. **b**, As in **a**, but from 0 to 40 Ma. Sediments deposited in the Indus Fan at circa 30 Ma would have had  $^{87}\text{Sr}/^{86}\text{Sr}$  ratios comparable to those measured in the Khanneshin samples. This implies that sediment recycling through the Makran subduction zone took less than 27 Myr.

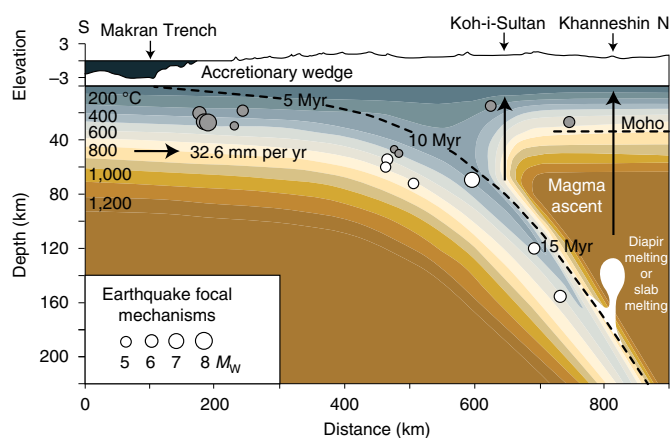


**Fig. 4 | Schematic cross-section of the eastern Makran subduction zone.** Khanneshin magmas are probably derived from subducted sediments that melted near the top of the subducting slab or in buoyant diapirs that ascended into the mantle wedge. Slab depths and the thermal structure are based on earthquake focal mechanisms<sup>17</sup> and thermal modelling<sup>30</sup>, respectively. The black dashed line along the top of the subducting Arabian plate represents the trajectory of subducted Indus Fan material and the time elapsed since entering the trench. Earthquakes with focal mechanisms < 50 km deep are shown as grey circles.

beneath the Khanneshin volcano would take 17 Myr (Fig. 4). Thus, sediment transfer to the trench and the ascent of recycled materials from the slab presumably lasted < 10 Myr combined.

### Recycled carbon resides in continental carbonatites

There is increasing isotopic evidence that some carbonatitic magmas worldwide contain recycled crustal material. Radiogenic isotope systematics suggest that carbonatites derive from either marine sedimentary carbon recycled through subcontinental lithosphere or deeply subducted carbonated oceanic crust that returns from either the transition zone or from the core–mantle boundary<sup>14</sup>. The role of recycling is confirmed by calcium isotopes<sup>16</sup> and boron isotopes<sup>15</sup>, but the recycling scenarios invoked by these studies require timescales of 100–1,000 Myr. The Khanneshin volcano is evidence that sedimentary carbon recycles to and from typical postarc depths on short timescales (that is, < 100 Myr). Low-volume carbonatitic melts cannot survive metasomatic entrapment<sup>43</sup> and rapid devolatilization<sup>44</sup> during ascent, so the exceptionally high sedimentary carbon flux into the Makran Trench may have been necessary to produce carbonatitic magmas voluminous enough to reach the surface. This might explain why carbonatite volcanism occurs in the Makran subduction zone, but not elsewhere on Earth<sup>13</sup>.

Globally, subducting carbon inputs appear to be larger than volcanic arc outputs<sup>6,8</sup>. This imbalance is especially pronounced for the Makran and Andaman–Burma subduction zones, where the Himalaya-derived Indus and Bengal fans may transport > 12 Mt per yr of carbon—roughly 7% of the global subducting carbon flux<sup>1</sup>—into the mantle wedge<sup>9</sup>. These subduction zones are associated with only one active volcano that outgasses substantial quantities of CO<sub>2</sub> and SO<sub>2</sub> (Barren Island, India<sup>45</sup>), but there are several volcanic centres that have been active during the Quaternary period (including Bazman, Taftan and Koh-i-Sultan in the Makran arc) that are potential sources of diffuse volcanic CO<sub>2</sub> and for which the modern and historical fluxes are unknown<sup>46</sup>. If Khanneshin volcanic CO<sub>2</sub> emissions were comparable to those of the Oldoinyo Lengai carbonatite volcano in Tanzania<sup>17</sup>, it could have contributed 2.4 Mt per yr. Currently, most volcanic CO<sub>2</sub> emissions in the region may come from the Tengchong volcanic field, China (4.5–7.1 Mt per yr (ref. 48)), which is related to the subduction of the

Burma slab<sup>49</sup>. Unless there are major CO<sub>2</sub> sources undetected by satellite measurements<sup>45</sup>, the Makran and Andaman–Burma carbon inputs are probably not balanced by volcanic gas emissions, unlike in the Java and Sumatra subduction zones<sup>50</sup>. This suggests that the return of subducted carbon to the atmosphere is inefficient in subduction zones with the highest sedimentary carbon fluxes. In such settings, the carbon inputs must be balanced by carbon mixed into the convecting mantle<sup>5</sup>, the storage of carbon in lithospheric reservoirs<sup>6</sup> or both. The Khanneshin volcano is evidence that subducted carbon can rapidly return to lithospheric reservoirs. It may be a rare surface expression of long-lived carbon reservoirs that form via carbonatitic magmatism in the rear-arc lithosphere.

### Online content

Any methods, additional references, Nature Research reporting summaries, source data, extended data, supplementary information, acknowledgements, peer review information; details of author contributions and competing interests; and statements of data and code availability are available at <https://doi.org/10.1038/s41561-021-00764-7>.

Received: 15 December 2020; Accepted: 10 May 2021;

Published online: 01 July 2021

### References

- Plank, T. & Manning, C. E. Subducting carbon. *Nature* **574**, 343–352 (2019).
- Behn, M. D., Kelemen, P. B., Hirth, G., Hacker, B. R. & Massonne, H.-J. Diapirs as the source of the sediment signature in arc lavas. *Nat. Geosci.* **4**, 641–646 (2011).
- Thomsen, T. B. & Schmidt, M. W. Melting of carbonated pelites at 2.5–5.0 GPa, silicate–carbonate liquid immiscibility, and potassium–carbon metasomatism of the mantle. *Earth Planet. Sci. Lett.* **267**, 17–31 (2008).
- Mallik, A. & Dasgupta, R. Reactive infiltration of MORB–eclogite-derived carbonated silicate melt into fertile peridotite at 3 GPa and genesis of alkaline magmas. *J. Petrol.* **54**, 2267–2300 (2013).
- Hirschmann, M. M. Comparative deep Earth volatile cycles: the case for C recycling from exosphere/mantle fractionation of major (H<sub>2</sub>O, C, N) volatiles and from H<sub>2</sub>O/Ce, CO<sub>2</sub>/Ba, and CO<sub>2</sub>/Nb exosphere ratios. *Earth Planet. Sci. Lett.* **502**, 262–273 (2018).
- Kelemen, P. B. & Manning, C. E. Reevaluating carbon fluxes in subduction zones, what goes down, mostly comes up. *Proc. Natl Acad. Sci. USA* **112**, E3997–E4006 (2015).
- Dasgupta, R. Ingassing, storage, and outgassing of terrestrial carbon through geologic time. *Rev. Mineral. Geochem.* **75**, 183–229 (2013).
- Aiuppa, A., Fischer, T. P., Plank, T. & Bani, P. CO<sub>2</sub> flux emissions from the Earth's most actively degassing volcanoes, 2005–2015. *Sci. Rep.* **9**, 5442 (2019).
- Clift, P. D. A revised budget for Cenozoic sedimentary carbon subduction. *Rev. Geophys.* **55**, 97–125 (2017).
- Burg, J.-P. Geology of the onshore Makran accretionary wedge: synthesis and tectonic interpretation. *Earth Sci. Rev.* **185**, 1210–1231 (2018).
- Pang, K.-N., Chung, S.-L., Zarrinkoub, M. H., Chiu, H.-Y. & Li, X.-H. On the magmatic record of the Makran arc, southeastern Iran: insights from zircon U–Pb geochronology and bulk-rock geochemistry. *Geochem. Geophys. Geosyst.* **15**, 2151–2169 (2014).
- Hammouda, T. & Keshav, S. Melting in the mantle in the presence of carbon: review of experiments and discussion on the origin of carbonatites. *Chem. Geol.* **418**, 171–188 (2015).
- Bell, K. & Simonetti, A. Source of parental melts to carbonatites—critical isotopic constraints. *Mineral. Petrol.* **98**, 77–89 (2010).
- Hoernle, K., Tilton, G., Le Bas, M. J., Duggen, S. & Garbe-Schönberg, D. Geochemistry of oceanic carbonatites compared with continental carbonatites: mantle recycling of oceanic crustal carbonate. *Contrib. Mineral. Petrol.* **142**, 520–542 (2002).
- Hullett, S. R., Simonetti, A., Rasbury, E. T. & Hemming, N. G. Recycling of subducted crustal components into carbonatite melts revealed by boron isotopes. *Nat. Geosci.* **9**, 904–908 (2016).
- Amsellem, E. et al. Calcium isotopic evidence for the mantle sources of carbonatites. *Sci. Adv.* **6**, eaba3269 (2020).
- Penney, C. et al. Megathrust and accretionary wedge properties and behaviour in the Makran subduction zone. *Geophys. J. Int.* **209**, 1800–1830 (2017).
- Smith, G., McNeill, L., Henstock, T. J. & Bull, J. The structure and fault activity of the Makran accretionary prism. *J. Geophys. Res. Solid Earth* **117**, B07407 (2012).

19. Pang, K.-N., Teng, F.-Z., Sun, Y., Chung, S.-L. & Zarrinkoub, M. H. Magnesium isotopic systematics of the Makran arc magmas, Iran: implications for crust-mantle Mg isotopic balance. *Geochim. Cosmochim. Acta* **78**, 110–121 (2020).
20. Motaghi, K., Shabani, E. & Nozad-Khalil, T. Deep structure of the western coast of the Makran subduction zone, SE Iran. *Tectonophysics* **776**, 228314 (2020).
21. Simmons, N. A., Myers, S. C. & Johannesson, G. Global-scale P wave tomography optimized for prediction of teleseismic and regional travel times for Middle East events: 2. Tomographic inversion. *J. Geophys. Res. Solid Earth* **116**, B04305 (2011).
22. Al-Lazki, A. I., Al-Damegh, K. S., El-Hadidy, S. Y., Ghods, A. & Tatar, M. Pn-velocity structure beneath Arabia–Eurasia Zagros collision and Makran subduction zones. *Geol. Soc. Spec. Publ.* **392**, 45–60 (2014).
23. Tucker, R. D., Belkin, H. E., Schulz, K. J., Peters, S. G. & Buttleman, K. P. *Rare Earth Element Mineralogy, Geochemistry, and Preliminary Resource Assessment of the Khanneshin Carbonatite Complex, Helmand Province, Afghanistan* (US Geological Survey, 2011).
24. Tucker, R. D. et al. A major light rare-earth element (LREE) resource in the Khanneshin carbonatite complex, southern Afghanistan. *Econ. Geol.* **107**, 197–208 (2012).
25. Woolley, A. R. & Church, A. A. Extrusive carbonatites: a brief review. *Lithos* **85**, 1–14 (2005).
26. Ayuso, R. et al. Preliminary radiogenic isotope study on the origin of the Khanneshin carbonatite complex, Helmand Province, Afghanistan. *J. Geochem. Explor.* **133**, 6–14 (2013).
27. Horton, F., Nielsen, S., Shu, Y., Gagnon, A. & Blusztajn, J. Thallium isotopes reveal brine activity during carbonatite magmatism. *Geochem. Geophys. Geosyst.* **22**, e2020GC009472 (2021).
28. Maggi, A., Jackson, J. A., Priestley, K. & Baker, C. A re-assessment of focal depth distributions in southern Iran, the Tien Shan and northern India: do earthquakes really occur in the continental mantle? *Geophys. J. Int.* **143**, 629–661 (2000).
29. Saadat, S. & Stern, C. R. Petrochemistry and genesis of olivine basalts from small monogenetic parasitic cones of Bazman stratovolcano, Makran arc, southeastern Iran. *Lithos* **125**, 607–619 (2011).
30. Smith, G. L., McNeill, L. C., Wang, K., He, J. & Henstock, T. J. Thermal structure and megathrust seismogenic potential of the Makran subduction zone. *Geophys. Res. Lett.* **40**, 1528–1533 (2013).
31. Robert, A. M., Fernández, M., Jiménez-Munt, I. & Vergés, J. Lithospheric structure in Central Eurasia derived from elevation, geoid anomaly and thermal analysis. *Geol. Soc. Spec. Publ.* **427**, 271–293 (2017).
32. Gonzalez, C. M., Górczyk, W. & Gerya, T. V. Decarbonation of subducting slabs: insight from petrological–thermomechanical modeling. *Gondwana Res.* **36**, 314–332 (2016).
33. Jarrard, R. D. & Lyle, M. High-resolution geochemical variations at sites 723, 728, and 731: a comparison of X-ray fluorescence and geochemical logs. *Proc. Ocean Drill. Prog. Sci. Results* **117**, 473–498 (1991).
34. Tsuno, K. & Dasgupta, R. The effect of carbonates on near-solidus melting of pelite at 3 GPa: Relative efficiency of H<sub>2</sub>O and CO<sub>2</sub> subduction. *Earth Planet. Sci. Lett.* **319**, 185–196 (2012).
35. White, W. M. & Hofmann, A. W. Sr and Nd isotope geochemistry of oceanic basalts and mantle evolution. *Nature* **296**, 821–825 (1982).
36. White, W. M. Isotopes, DUPAL, LLSVPs, and anekantavada. *Chem. Geol.* **419**, 10–28 (2015).
37. Clift, P. D. et al. Nd and Pb isotope variability in the Indus River System: implications for sediment provenance and crustal heterogeneity in the Western Himalaya. *Earth Planet. Sci. Lett.* **200**, 91–106 (2002).
38. Whitney, J. W. *Geology, Water and Wind in the Lower Helmand Basin, Southern Afghanistan* (US Geological Survey, 2006).
39. Artemieva, I. M. Global 1°×1° thermal model TC1 for the continental lithosphere: implications for lithosphere secular evolution. *Tectonophysics* **416**, 245–277 (2006).
40. Clift, P. D. et al. Development of the Indus Fan and its significance for the erosional history of the Western Himalaya and Karakoram. *Geol. Soc. Am. Bull.* **113**, 1039–1051 (2001).
41. McArthur, J. M., Howarth, R. J. & Shields, G. A. in *The Geologic Time Scale* (eds Gradstein, M. A. et al.) 127–144 (Elsevier, 2012).
42. Platt, J. P., Leggett, J. K., Young, J., Raza, H. & Alam, S. Large-scale sediment underplating in the Makran accretionary prism, southwest Pakistan. *Geology* **13**, 507–511 (1985).
43. Sleep, N. H. Stagnant lid convection and carbonate metasomatism of the deep continental lithosphere. *Geochem. Geophys. Geosyst.* **10**, Q11010 (2009).
44. Wyllie, P. J. & Huang, W.-L. Peridotite, kimberlite, and carbonatite explained in the system CaO-MgO-SiO<sub>2</sub>-CO<sub>2</sub>. *Geology* **3**, 621–624 (1975).
45. Carn, S. A., Fioletov, V. E., McLinden, C. A., Li, C. & Krotkov, N. A. A decade of global volcanic SO<sub>2</sub> emissions measured from space. *Sci. Rep.* **7**, 44095 (2017).
46. Werner, C. et al. in *Deep Carbon: Past to Present* (eds Orcutt, B. N. et al.) 188–236 (Cambridge Univ. Press, 2019).
47. Brantley, S. L. & Koepnick, K. W. Measured carbon dioxide emissions from Oldoinyo Lengai and the skewed distribution of passive volcanic fluxes. *Geology* **23**, 933–936 (1995).
48. Zhang, M. et al. Magma-derived CO<sub>2</sub> emissions in the Tengchong volcanic field, SE Tibet: implications for deep carbon cycle at intra-continent subduction zone. *J. Asian Earth Sci.* **127**, 76–90 (2016).
49. Huang, J. & Zhao, D. High-resolution mantle tomography of China and surrounding regions. *J. Geophys. Res. Solid Earth* **111**, B09305 (2006).
50. House, B. M., Bebout, G. E. & Hilton, D. R. Carbon cycling at the Sunda margin, Indonesia: a regional study with global implications. *Geology* **47**, 483–486 (2019).

**Publisher's note** Springer Nature remains neutral with regard to jurisdictional claims in published maps and institutional affiliations.

© The Author(s), under exclusive licence to Springer Nature Limited 2021

## Methods

**Strontium isotope measurements.** Carbonatite samples were powdered by hand using an agate mortar and pestle. Between 5 and 10 mg of each sample was dissolved in a 3:1 mixture of HF and HNO<sub>3</sub>. Strontium was separated and purified from the samples using Sr-Spec resin (Eichrom). Strontium isotopic measurements were performed using a Thermo-Finnigan Neptune ICP-MS instrument at Woods Hole Oceanographic Institution. Isobaric interferences of <sup>87</sup>Kr on <sup>87</sup>Sr and <sup>86</sup>Kr on <sup>86</sup>Sr were corrected for by monitoring <sup>82</sup>Kr, <sup>83</sup>Kr and <sup>85</sup>Rb and by applying a mass-bias correction using an exponential relationship<sup>51</sup>. The internal precision for strontium isotopic measurements was 6–24 ppm. Raw strontium results are normalized using standard SRM987 (<sup>87</sup>Sr/<sup>86</sup>Sr = 0.7102140). Standard NBS987 was reproducible to within 25 ppm. See Extended Data Table 1 for strontium isotopic results.

**<sup>40</sup>Ar–<sup>39</sup>Ar geochronology.** At the Oregon State University Argon Geochronology Laboratory, three phlogopite aliquots were cleaned for 30 min in 200 proof HPLC-grade acetone and for 30 min in ethyl alcohol, before being rinsed four times with triple-distilled water and dried at 55 °C for 12 h. The samples were irradiated in the Oregon State University TRIGA reactor for 6 h, along with Fish Canyon Tuff sanidines<sup>52</sup> that served as flux monitors. Following the procedures described in ref. <sup>53</sup>, portions of each phlogopite aliquot (3.882, 9.351 and 4.251 mg for aliquots 1–3, respectively) were loaded in copper planchettes and step heated by rastering a 30 W Synrad CO<sub>2</sub> laser beam across each sample under ultrahigh vacuum. Reactive gases were cleaned with AP10 Zr–Al SAES getters at 450 °C and 21 °C before the argon was inlet into an ARGUS VI multicollector mass spectrometer for analysis. Plateau ages (Extended Data Fig. 6), based on contiguous extraction steps with apparent <sup>40</sup>Ar–<sup>39</sup>Ar dates that are indistinguishable at the 95% confidence interval, were calculated using ArArCALC v.2.6.2 software<sup>54</sup> using the decay constant  $(5.530 \pm 0.097) \times 10^{-10}$  per yr ( $2\sigma$ ) from ref. <sup>55</sup> and corrected by ref. <sup>56</sup>. See Supplementary Data 1, 2 and 3 for the complete results from the Argon Geochronology Laboratory.

## Data availability

The Ar–Ar geochronology and strontium isotope results are publicly available via EarthChem (<https://doi.org/10.26022/IEDA/111960>).

## References

- Jackson, M. G. & Hart, S. R. Strontium isotopes in melt inclusions from Samoan basalts: implications for heterogeneity in the Samoan plume. *Earth Planet. Sci. Lett.* **245**, 260–277 (2006).
- Kuiper, K. F. et al. Synchronizing rock clocks of Earth history. *Science* **320**, 500–504 (2008).
- Cahoon, E. B., Streck, M. J., Koppers, A. A. & Miggins, D. P. Reshuffling the Columbia River Basalt chronology—Picture Gorge Basalt, the earliest- and longest-erupting formation. *Geology* **48**, 348–352 (2020).
- Koppers, A. A. ArArCALC—software for <sup>40</sup>Ar/<sup>39</sup>Ar age calculations. *Comput. Geosci.* **28**, 605–619 (2002).
- Steiger, R. H. & Jäger, E. Subcommission on geochronology: convention on the use of decay constants in geo- and cosmochronology. *Earth Planet. Sci. Lett.* **36**, 359–362 (1977).
- Min, K., Mundil, R., Renne, P. R. & Ludwig, K. R. A test for systematic errors in <sup>40</sup>Ar/<sup>39</sup>Ar geochronology through comparison with U/Pb analysis of a 1.1-Ga rhyolite. *Geochim. Cosmochim. Acta* **64**, 73–98 (2000).
- Alkhazov, V. Y., Atakishiyev, Z. M. & Azimi, N. A. Geology and mineral resources of the early Quaternary Khanneshin carbonatite volcano (Southern Afghanistan). *Int. Geol. Rev.* **20**, 281–285 (1978).
- Plank, T. & Langmuir, C. H. The chemical composition of subducting sediment and its consequences for the crust and mantle. *Chem. Geol.* **145**, 325–394 (1998).
- McDonough, W. F. & Sun, S. S. The composition of the Earth. *Chem. Geol.* **120**, 223–253 (1995).

## Acknowledgements

R. Seal at the US Geological Survey granted access to the samples, which were collected by the US Geological Survey and the US Department of Defense Task Force for Business and Stability Operations personnel led by R. Tucker and E. King. The Afghanistan Geological Survey provided access to Soviet reports about the Khanneshin volcano that were essential for the fieldwork. The Afghanistan Ministry of Mines and Petroleum granted permission for sample collection. Combined Forces Special Operations Command - Afghanistan provided logistics and security support. At the time of sample collection, F.H. was an employee of TFBSO. J. Blusztajn and D. Miggins carried out the strontium isotope analyses and Ar–Ar geochronology, respectively. Discussions with S. Nielsen and G. Gaetani improved this paper. This project was supported by the Woods Hole Oceanographic Institution Independent Research & Development Program and a National Science Foundation grant (EAR number 1911699) awarded to F.H.

## Competing interests

The author declares no competing interests.

## Additional information

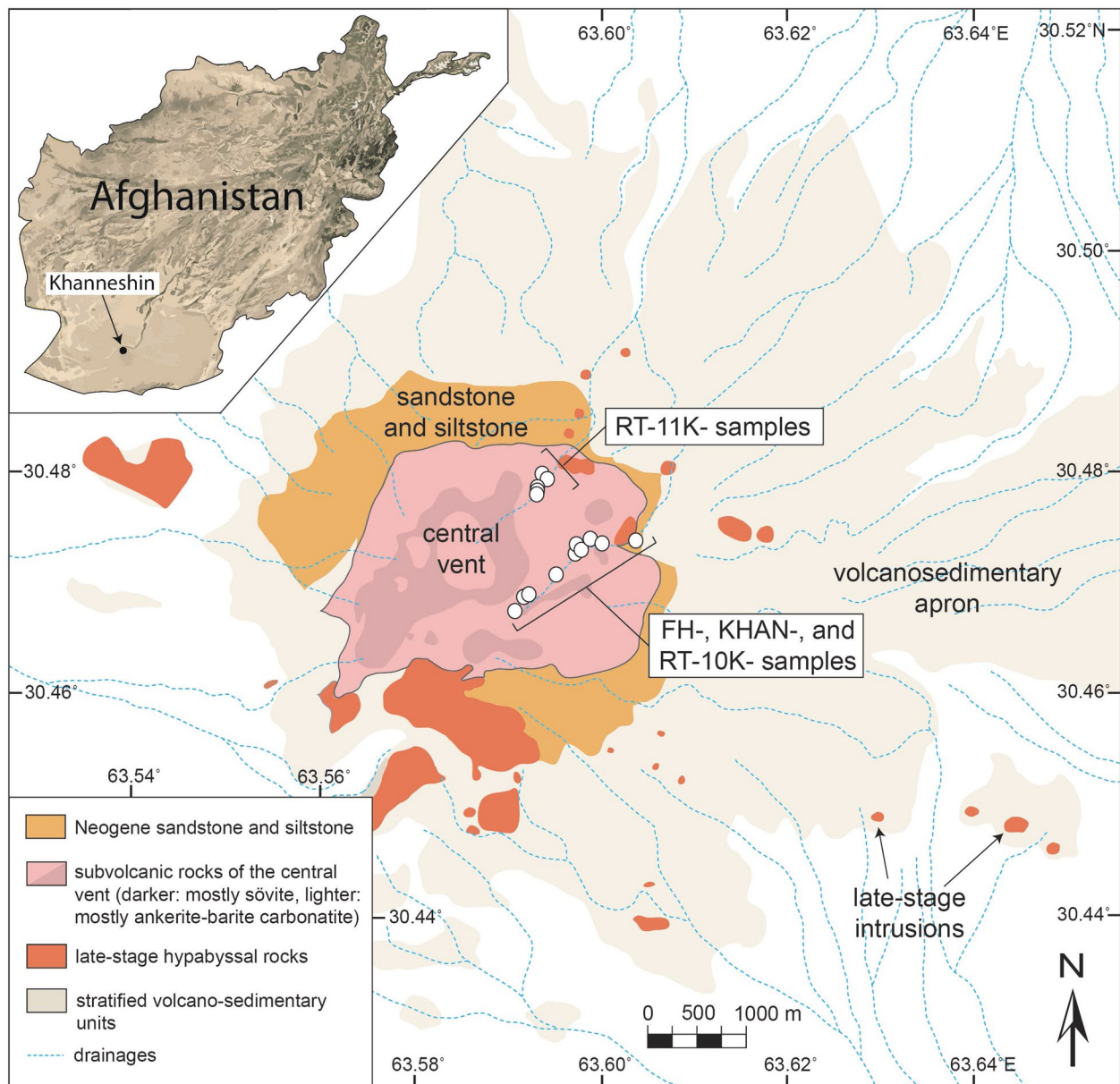
**Extended data** is available for this paper at <https://doi.org/10.1038/s41561-021-00764-7>.

**Supplementary information** The online version contains supplementary material available at <https://doi.org/10.1038/s41561-021-00764-7>.

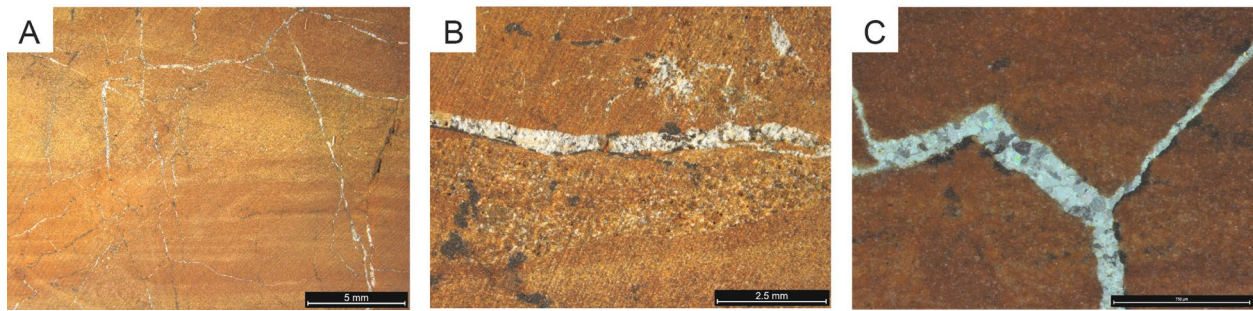
**Correspondence and requests for materials** should be addressed to F.H.

**Peer review information** *Nature Geoscience* thanks Elsa Amsellem, Kwan-Nang Pang and Sabin Zahirovic for their contribution to the peer review of this work. Primary Handling Editor: Rebecca Neely.

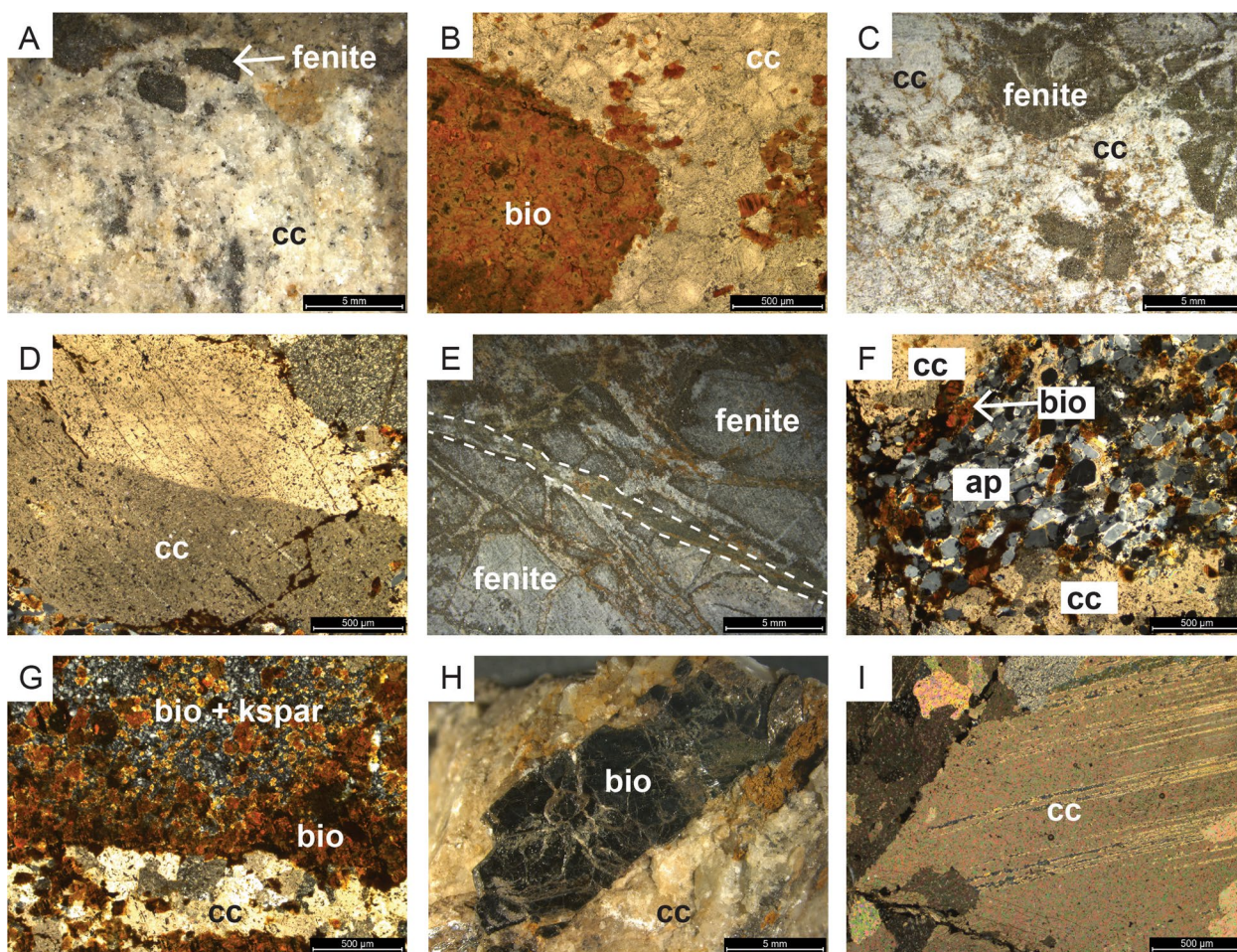
**Reprints and permissions information** is available at [www.nature.com/reprints](http://www.nature.com/reprints).



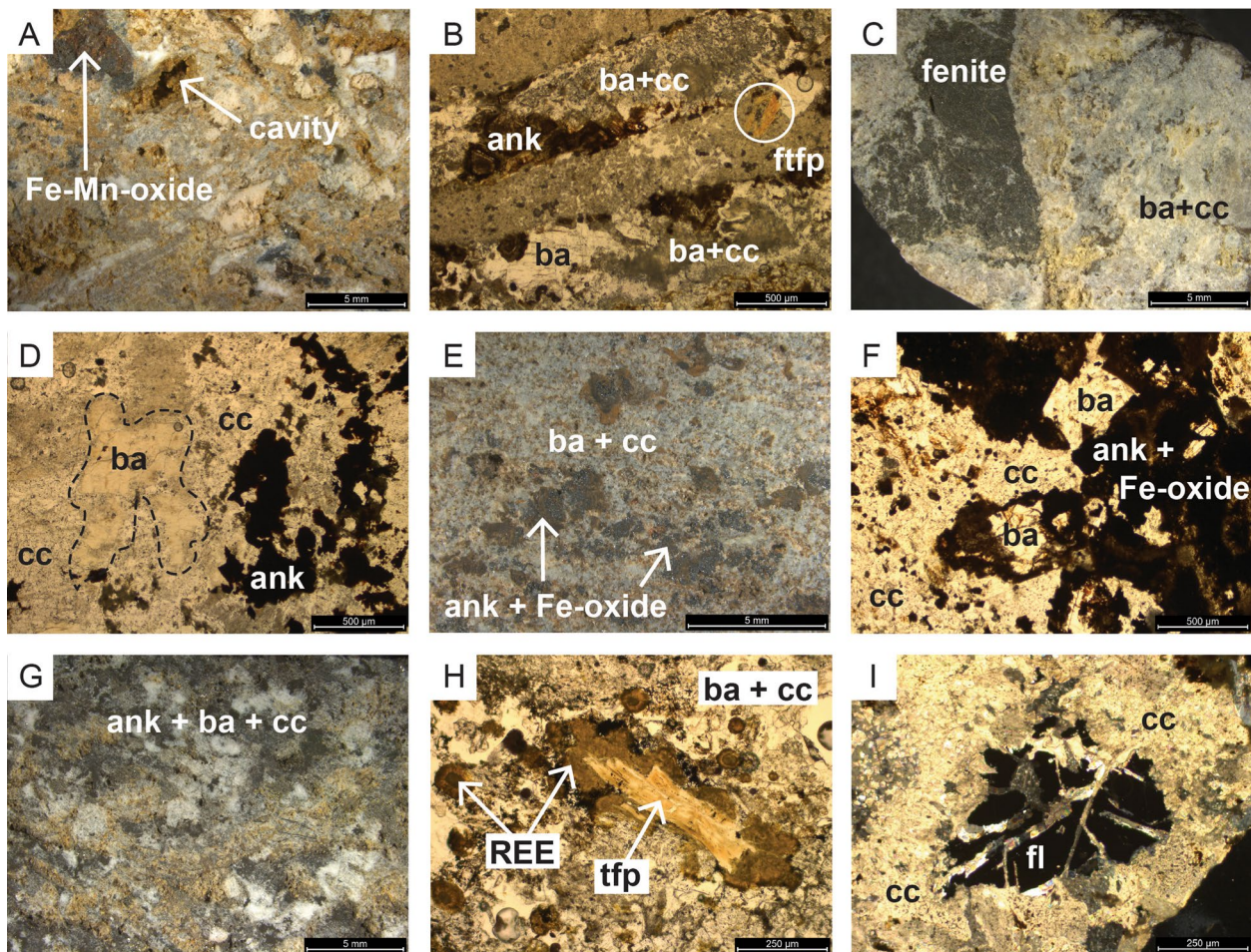
**Extended Data Fig. 1 | Geologic map of the Khanneshin volcano showing sample locations.** The core of the central vent consists mostly of sövite with abundant fenite xenoliths. Outer portions of the central vent are composed mostly of ankerite-barite carbonatite, inferred to be younger than the sövite because they host sövite xenoliths. Samples (white circles) were collected from two drainages that exit the massif to the northeast. This figure is a modified version of the geologic map published by ref. <sup>27</sup>, which is based on ref. <sup>57</sup> and ref. <sup>23</sup>.



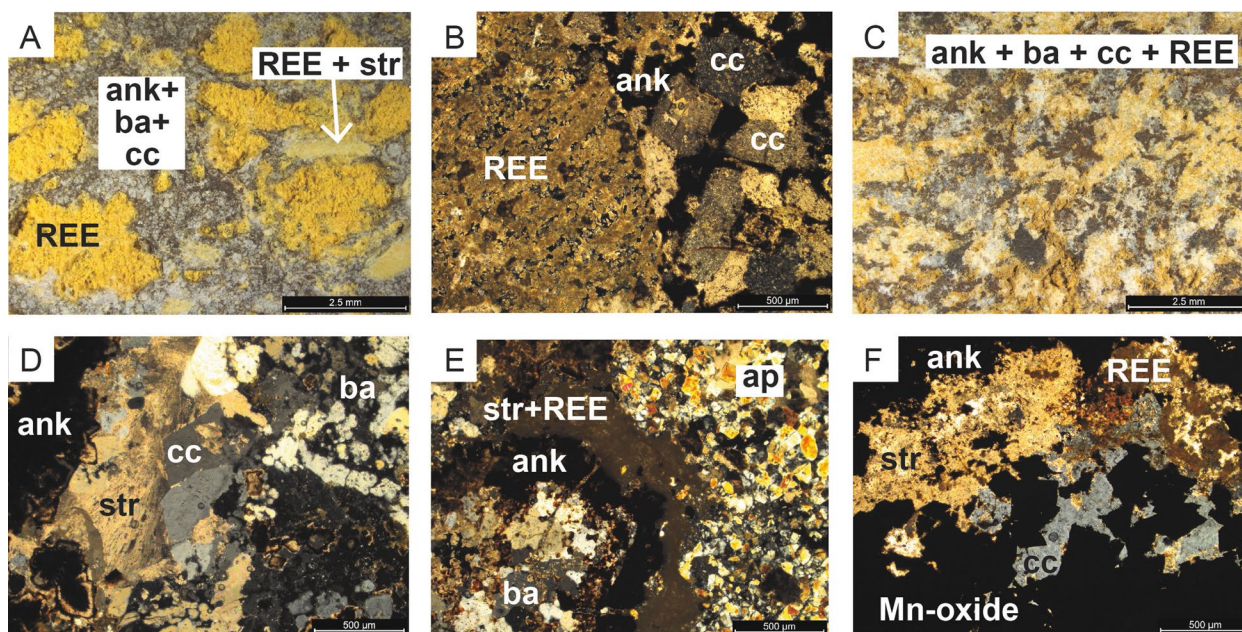
**Extended Data Fig. 2 | Mineralogy and petrology of sandstone sample FH-10KH-10.** **a**, Sawed surface image. The sedimentary clasts are dominantly K-feldspar. Bedding is defined by alternating sandstone and siltstone layers, of which the latter appear darker because they have more interstitial Fe-oxide. The rock is brecciated and crosscut by calcium carbonate veins. **B**, Closer inspection of a carbonate vein reveals anastomosing networks of smaller veins extending into the sandstone. Beneath the large vein is a porous metasomatized region where cavities are partially filled by carbonate minerals, including minor amounts of REE-carbonates. **C**, Thin section photomicrograph. Along calcium carbonate vein margins are secondary Fe-Mn-oxides (black).



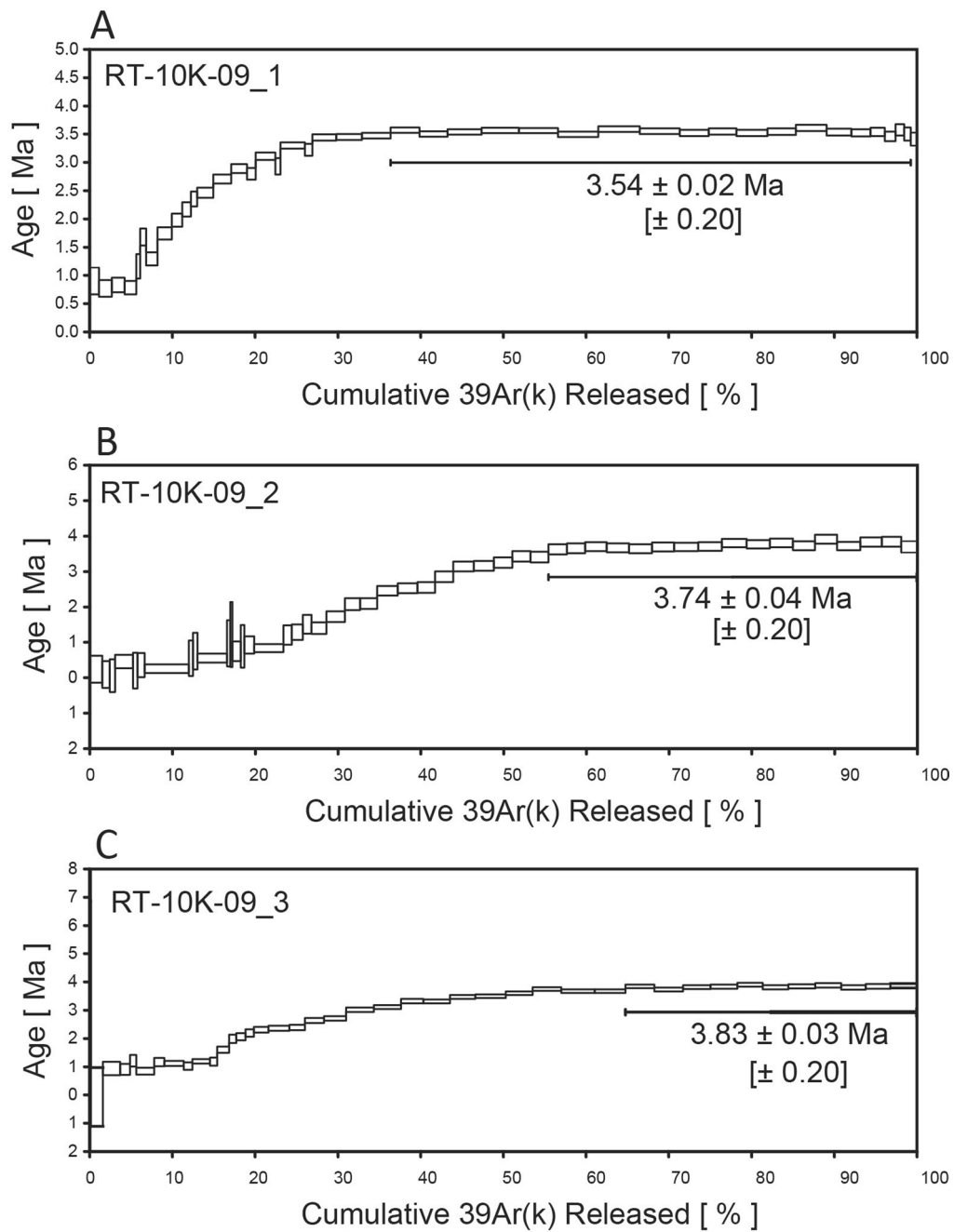
**Extended Data Fig. 3 | Mineralogy and petrology of representative sövite samples.** **a**, KHAN-1, hand sample image. Medium- to coarse-grained calcite carbonatite contains fine-grained biotite. Three small fenite xenoliths are visible in the upper left. **b**, KHAN-1, PPL. Small fenite xenoliths, like the one imaged here, are composed of biotite. They share sharp and diffuse boundaries with the surrounding calcite matrix. **c**, KHAN-2, sawed surface image. Larger fenite xenoliths are highly brecciated and crosscut by calcite veins. **d**, KHAN-2, XPL. Large twinned calcite crystal with Fe-oxide and biotite inclusions. Contact twinning separates the upper and lower portions of the crystal, both of which have subtle lamellae twins. **e**, KHAN-2, sawed surface image. Large fenite xenoliths have brecciated textures and are crosscut by multiple generations of veins. The white veins are calcite and the green vein, bound by dashed lines, is mostly apatite. **f**, KHAN-2, XPL. Apatite also forms clusters with biotite in the calcite matrix of sövite samples. **g**, KHAN-2, XPL. Large brecciated fenite xenoliths have biotite-rich zones adjacent to calcite veins and fine-grained interiors composed of biotite and K-feldspar. **h**, RT-10K-09, hand sample image. This sövite contains large (>1 cm) phlogopite books intergrown with coarse calcium carbonate. **i**, RT-10K-09, XPL. Calcite twin lamellae are visible in this sample. Mineral abbreviations: ap = apatite, bio = biotite, cc = calcium carbonate, kfs = K-feldspar. Hand sample and sawed surface images were taken on a stereomicroscope. Thin section images were taken on a polarizing microscope under plain polarized light (PPL) or cross polarized light (XPL).



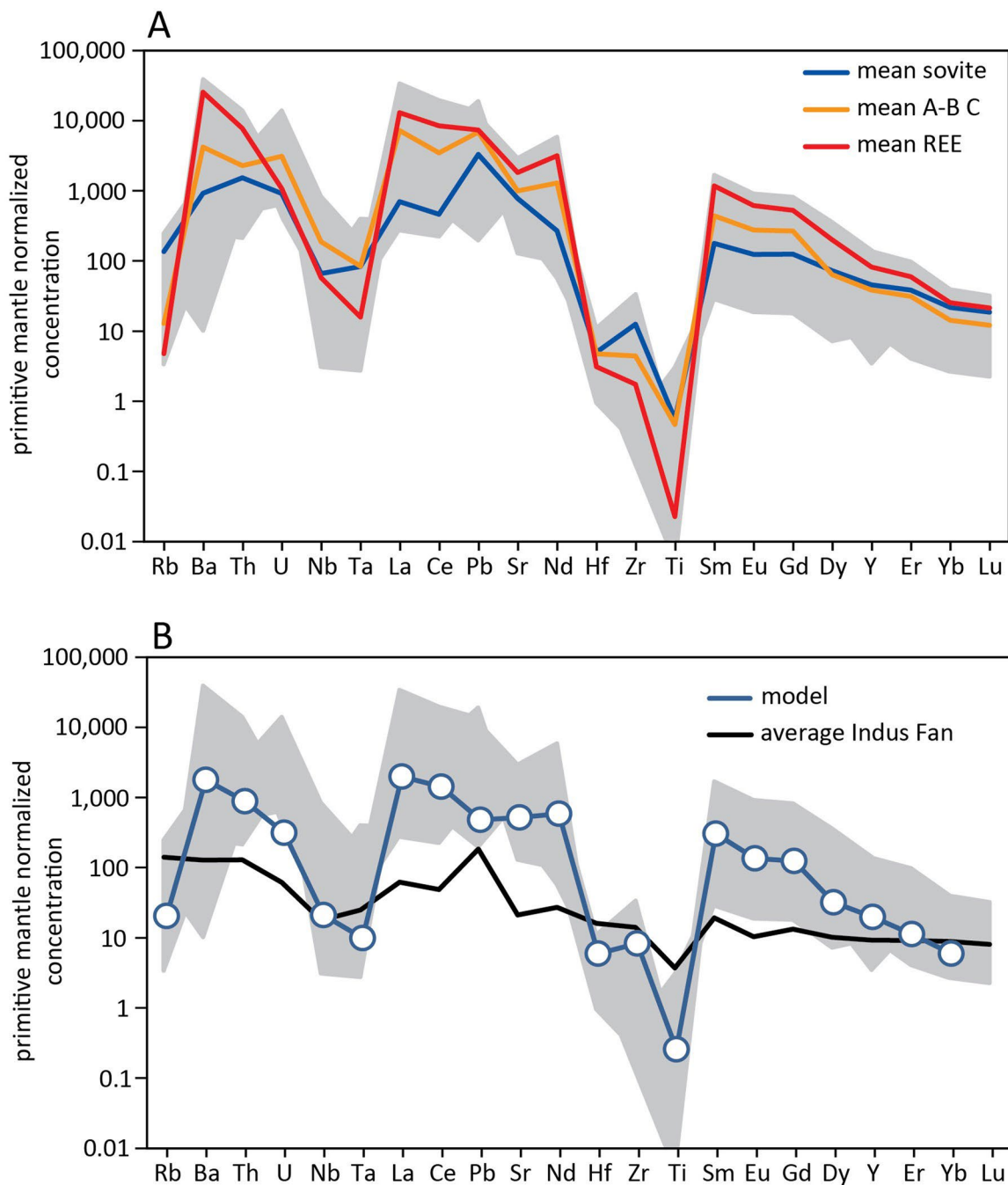
**Extended Data Fig. 4 | Mineralogy and petrology of representative ankerite-barite carbonatite samples.** **a**, FH-10K-08, sawed surface image. Lath-shaped intergrowths of barium, calcium carbonate, and ankerite form the matrix of this carbonatite. Fe-Mn oxides are present and REE-carbonates line the walls of cavities. **b**, FH-10K-08, PPL. The complex textures of the barium-calcium carbonate intergrowths—perhaps pseudomorphs after witherite—can be observed. Tetraferriphlogopite also exists in this sample as a minor phase. **c**, RT-10K-03, sawed surface image. Ankerite-barite carbonatites also contain fenite xenoliths, as shown here. REE carbonates appear yellow. **d**, RT-10K-03, PPL. Ankerite-barite carbonatites exhibit varied textures. Here, barite (outlined with a dashed line) and ankerite are surrounded by a finer-grained matrix of calcium carbonate. **e**, RT-10K-11, sawed surface image. Intergrowths of ankerite and Fe-oxides often form clusters. **f**, RT-10K-11, PPL. Tabular barite crystals occur in intimate association with ankerite and Fe-oxide. **g**, RT-10K-07, sawed surface image. Some samples are relatively homogeneous on the cm scale. Here, ankerite (grey) surrounds intergrowths of barite (white) and calcium carbonate (also white). Yellow regions contain REE minerals hosted in cavities. **h**, RT-10K-07, PPL. Tetraferriphlogopite is sometime rimmed by REE-carbonate minerals and tends to be associated with barite-calcium carbonate intergrowths. **i**, RT-10K-03, XPL. Solitary fluorite crystals (isotropic) exist in some ankerite-barite carbonatites and are rimmed by calcium carbonate. Mineral abbreviations: ank = ankerite, ba = barite, cc = calcium carbonate, fl = fluorite, tfp = tetraferriphlogopite, REE = rare earth element carbonate minerals.



**Extended Data Fig. 5 | Mineralogy and petrology of REE-rich ankerite barite carbonatites.** **a**, RT-11K-4A0, sawed surface image. Aggregates of yellow REE-carbonates in a matrix of ankerite, barite, and calcite. Clusters of REE-carbonate and strontianite form lighter yellow clusters. **b**, RT-11K-4A0, XPL. Contact between REE-carbonate aggregates and ankerite-barite-calcite matrix. **c**, RT-11K-5B3B, sawed surface image. Ankerite (dark brown patches) plus calcium carbonate (grey) zones alternate with barite, strontianite, and REE-carbonate aggregates. **d**, RT-11K-5B3B, XPL. Spherulitic acicular strontianite occurs in association with ankerite, calcium carbonate, and barite. **e**, RT-11K-2B, XPL. In some cases, subhedral domains of barite and ankerite are rimmed by zones of ankerite, strontianite plus REE-carbonates, and apatite. **f**, RT-11K-5B6C, XPL. Mn oxides occur as veins and clusters. Here, tabular Mn-oxide in a vein contains interstitial calcium carbonate, which grades into intergrowths of strontianite and REE-carbonate minerals. Mineral abbreviations: ank = ankerite, ba = barite, cc = calcium carbonate, REE = rare earth element carbonate minerals, str = strontianite.



**Extended Data Fig. 6 |  $^{40}\text{Ar}/^{39}\text{Ar}$  plateau diagrams. a-c,** Step heating analyses of RT-10K-09 phlogopite aliquots 1-3, respectively.



**Extended Data Fig. 7 | Trace element model.** **a**, The trace element concentrations in the Khanneshin carbonatite samples vary by roughly 1–2 orders of magnitude for each element (grey shaded region). In general, sövite samples are less enriched than ankerite-barite carbonatites. Colored lines represent mean compositions for Khanneshin sövites and ankerite-barite carbonatites with (“REE”) and without (“A-B C”) abundant REE minerals. **b**, The modeled composition of carbonatitic melt derived from subducted Makran sedimentary material—assumed to equal average Indus Fan sediments<sup>58</sup>—and Khanneshin carbonatite samples (grey shaded region) have similar trace element patterns. The model assumes that 30% melting of subducted sediments produced a carbonated silicate magma that separated into immiscible carbonatitic and silicate magmas during ascent. See Supplementary Information text for details. All values are normalized to primitive mantle<sup>59</sup>.

**Extended Data Table 1** |  $^{87}\text{Sr}/^{86}\text{Sr}$  results for 20 Khanneshin carbonatite samples and one sandstone

Strontium isotope results for the Khanneshin samples.

Sample	Description	Latitude	Longitude	$^{87}\text{Sr}/^{86}\text{Sr}$	Internal error ( $\pm 2$ SE)
KHAN-1	sövite	30.4738	63.5996	0.707979	0.000024
KHAN-2	sövite	30.4734	63.6011	0.707992	0.000020
KHAN-3	sövite	30.4732	63.5989	0.708061	0.000008
FH-10K-8	ankerite-barite carbonatite	30.4685	63.5929	0.708022	0.000020
FH-10KH-10	sandstone	30.4738	63.6046	0.708048	0.000020
RT-10K-03	ankerite-barite carbonatite	30.4729	63.5979	0.708026	0.000024
RT-10K-07	ankerite-barite carbonatite	30.4685	63.5930	0.708039	0.000013
RT-10K-09	sövite	30.4708	63.5959	0.708021	0.000015
RT-10K-11	ankerite-barite carbonatite	30.4735	63.5982	0.708026	0.000016
RT-10K-12	sövite	30.4738	63.5996	0.707976	0.000015
RT-10K-5D	ankerite-barite carbonatite	30.4688	63.5936	0.708034	0.000016
RT10K-6E	sövite	30.4671	63.5922	0.708013	0.000010
RT-11K-01	ankerite-barite carbonatite	30.4797	63.5949	0.708016	0.000014
RT-11K-2B2	ankerite-barite carbonatite	30.4792	63.5954	0.707972	0.000006
RT-11K-4A0	ankerite-barite carbonatite	30.4784	63.5945	0.708025	0.000012
RT-11K-5A1	ankerite-barite carbonatite	30.4782	63.5945	0.708008	0.000016
RT-11K-5B1A	ankerite-barite carbonatite	30.4782	63.5945	0.708000	0.000007
RT-11K-5B3B	ankerite-barite carbonatite	30.4782	63.5945	0.708028	0.000020
RT-11K-5B4	ankerite-barite carbonatite	30.4782	63.5945	0.708007	0.000020
RT-11K-5B6C	ankerite-barite carbonatite	30.4782	63.5945	0.707925	0.000010
RT-11K-6	ankerite-barite carbonatite	30.4781	63.5945	0.707919	0.000007

Extended Data Table 2 | Trace element abundances ( $\mu\text{g/g}$ ) in the Khanneshin samples<sup>23,27</sup>Trace element abundances ( $\mu\text{g/g}$ ) in the Khanneshin samples<sup>23,27</sup>. A-B C = Ankerite-barite carbonatite.

Sample	Description	Latitude	Longitude	Cs	Rb	Ba	Th	U	Nb	Ta	La	Ce	Pb	Sr	Nd	Hf	Zr	Ti	Sm	Eu	Gd	Dy	Y	Er	Yb	Lu
KHAN-1	sövite	30.4739	63.5997	4.90	69.7	5780	211	15	39	3.21	273	555	1380	17984	280	0.3	9	588	96	28	100	70	278	22.2	12.1	1.58
KHAN-2	sövite	30.4734	63.6011	9.04	143.6	9595	78	24	63	3.90	630	886	73	10991	296	0.9	39	1175	52	12	39	33	146	12.0	6.6	0.86
KHAN-3	sövite	30.4732	63.5989	0.56	7.1	1649	17	29	35	14.25	236	365	988	2505	120	0.3	6	3609	18	4	12	7	33	2.4	1.5	0.22
FH-10K-8	A-B C	30.4686	63.5930		2.7	721	97	29	36	3.10	5258	6364	560	19069	2157	1.7	59	84	190	72	214	15	21	10.4	3.8	0.60
FH-10KH-10	sandstone	30.4739	63.6047		40.6	318	91	5	215	1.20	43	111	106	2311	29	3.9	115	4161	10	4	15	21	147	10.8	9.5	1.40
RT-10K-03	A-B C	30.4729	63.5980		3.1	4651	91	34	59	2.10	6462	5999	190	23116	1430	1.6	44	276	119	50	198	25	109	12.7	5.0	0.70
RT-10K-07	A-B C	30.4686	63.5930		4.4	527	99	42	89	2.22	7351	5632	490	31940	1048	1.9	34	120	83	7	113	13	15	6.7	4.4	0.56
RT-10K-09	sövite	30.4709	63.5959		31.5	2840	76	17	29	2.16	459	896	29	17398	430	3.0	345	240	68	17	65	43	165	16.1	10.1	1.34
RT-10K-11	A-B C	30.4736	63.5982		4.2	5314	253	272	532	7.15	1921	3373	2383	13745	1396	3.0	81	444	209	53	178	65	290	19.5	10.1	1.30
RT-10K-12	sövite	30.4739	63.5997		5.5	7048	408	94	321	0.58	534	1705	1463	16004	473	0.9	17	438	88	25	96	74	412	24.4	14.2	1.95
RT-10K-5D	A-B C	30.4688	63.5936		3.1	1164	46	62	219	2.60	5049	6276	2722	13227	2285	1.6	52	132	207	71	227	18	25	10.7	2.5	0.30
RT10K-6E	sövite	30.4672	63.5923		37.9	66	37	13	46	1.45	181	377	152	6366	70	1.2	41	941	12	3	10	5	43	1.8	1.2	0.15
RT-11K-01	A-B C	30.4798	63.5949		4.0	196200	88	15	41	0.30	10300	14600	962	30470	2880	0.9		6	258	40	109	26	108	8.3	5.8	0.86
RT-11K-2B2	A-B C	30.4792	63.5955		2.0	210100	441	101	2	0.10	7980	11200	748	36380	3060	1.8	161	6	417	85	267	160	552	39.8	16.9	2.11
RT-11K-4A0	A-B C	30.4784	63.5945		2.0	49850	80	21	14	0.10	5550	7940	1210	47510	2160	0.3	33	6	231	38	92	23	112	8.6	8.4	1.34
RT-11K-5A1	A-B C	30.4782	63.5945		2.0	245900	864	9	28	0.40	5990	13000	660	25650	3690	1.3	20	6	507	110	349	181	465	32.8	12.6	1.57
RT-11K-5B1A	A-B C	30.4782	63.5945		2.0	237300	814	18	42	0.40	5380	11900	1420	37660	3600	1.4	18	6	508	109	352	201	575	42.3	15.8	1.80
RT-11K-5B3B	A-B C	30.4782	63.5945		2.0	227900	1070	28	72	0.20	6400	13300	622	49520	3990	1.5	15	6	626	136	431	236	594	38.2	12.7	1.52
RT-11K-5B4	A-B C	30.4782	63.5945	0.03	2.0	166371	656	15	32	0.29	4131	6792	908	13879	4387	0.3	3	102	564	127	402	234	462	41.6	14.6	1.62
RT-11K-5B6C	A-B C	30.4782	63.5945		6.0	50330	727	48	37	2.40	21000	31500	1950	49760	7090	0.5	21	60	657	102	274	47	162	11.0	8.3	1.36
RT-11K-6	A-B C	30.4781	63.5945		15.0	74900	504	16	16	0.80	16600	23000	1630	56190	5800	0.7	16	120	615	102	279	91	314	22.0	9.7	1.12